Supplementary Information
Integrated Optical Vortex Microcomb

Bo Chen,[1,*] Yueguang Zhou,[2,*] Peinian Huang,[1,*] Chaochao Ye,[2,*] Qian Cao,[3,*] Yang Liu,[2] Chanju Kim,[2] Kresten Yvind,[2] Jin Li,[4] Chunhua Dong,[4] Songnian Fu,[5] Qiwen Zhan,[3] Xuehua Wang,[1,†] Minhao Pu,[2,‡] and Jin Liu[1,§]

[1]*State Key Laboratory of Optoelectronic Materials and Technologies, School of Physics, School of Electronics and Information Technology, Sun Yat-sen University, Guangzhou, 510275, China*

[2]*DTU Electro, Technical University of Denmark, DK-2800 Lyngby, Denmark*

[3]*School of Optical-Electrical and Computer Engineering, University of Shanghai for Science and Technology, Shanghai, China*

[4]*CAS Key Laboratory of Quantum Information, University of Science and Technology of China, Hefei, 230026, China*

[5]*Institute of Advanced Photonics Technology, School of Information Engineering, Guangdong University of Technology, Guangzhou, 510006, China*

(Dated: November 2, 2022)

Device fabrication

The full device fabrication flow is shown in Fig. S(1). A 380-nm-thick AlGaAs layer is epitaxially grown on a GaAs wafer (100 surface) with sacrificial layer stacks (AlGaAs / InGaP / GaAs / InGaP / GaAs substrate). A 3-μm-thick silica (SiO_2) cladding is deposited on the GaAs wafer - on the AlGaAs surface - using plasma-enhanced chemical vapor deposition (PECVD). A substrate (InP) wafer is also deposited with a thin (10 nm) silica layer using PECVD to enhance the subsequent wafer bonding process. Both interfaces of the AlGaAs wafer and substrate wafer are spin-coated with adhesion promoter (AP3000); and benzocyclobutene (BCB) is spin-coated on the substrate wafer. The AlGaAs wafer and substrate wafer are bonded with a wafer bonding machine which applies a pressure of 6 bars at 250°C, in a vacuum environment. Once the bonding is completed, the GaAs substrate and the subsequent sacrificial layers (InGaP/GaAs/InGaP) are removed by wet etching – exposing the AlGaAs layer[1]. A mixed solution of sulfuric acid and hydrogen peroxide is used to remove the thick GaAs substrate. The thin layers of GaAs and InGaP are removed with citric acid/hydrogen solution and hydrogen chloride, respectively. A negative-tone electron-beam lithography (EBL) resist, hydrogen silsesquioxane (HSQ), is spin-coated on the AlGaAs thin film. We additionally deposit a 20-nm-thick aluminum layer (using thermal evaporator) on the HSQ layer to mitigate electron-beam charging effect during EBL writing process. The EBL system (JEOL JBX-9500FS) has an electron-beam acceleration voltage of 100 kV and the microresonator device patterns are exposed with an average dose of 11,000 μC/cm^2. An EBL resist developer is diluted with distilled water (AZ400K:H_2O = 1:3), and the solution etches the conductive aluminum layer and develops the HSQ. We use an inductively coupled plasma reactive ion etching (ICP-RIE, SPTS ICP) with a boron trichloride (BCl_3)-based gas chemistry to transfer the HSQ pattern to the AlGaAs thin film. Finally, we deposit a silica top cladding with a thickness of 3 μm using PECVD to encapsulate the AlGaAsOI microresonator device.

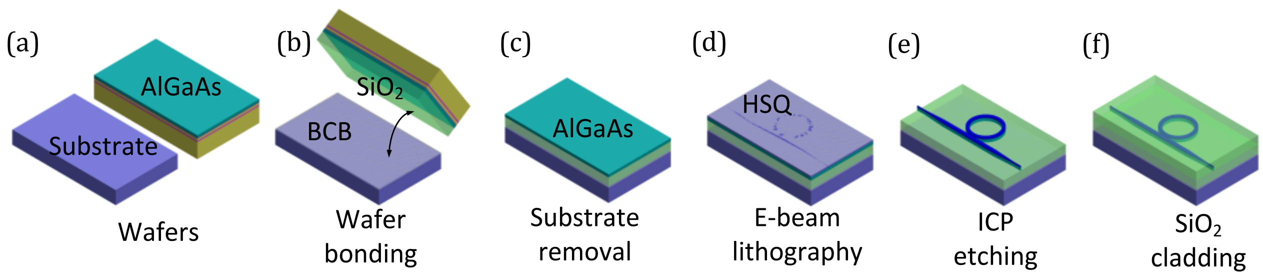

FIG. S1: Fabrication process flow of AlGaAs-on-insulator (AlGaAsOI) microresonator device.

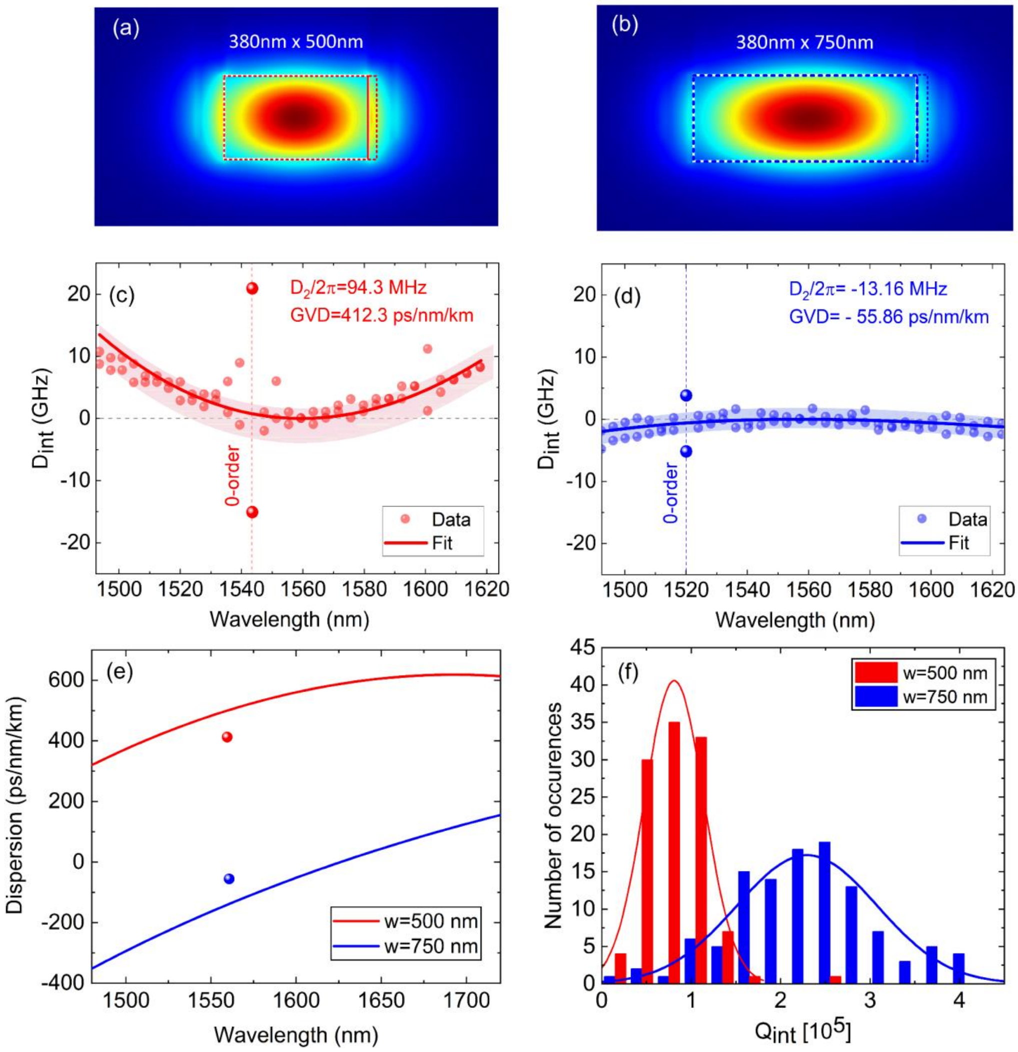

FIG. S2: **Dispersion and Q factors of AlGaAsOI OAM microresonators.** (a, b) TE_{00}-mode field intensity of the resonator waveguides. Resonator waveguide cross-section geometries are indicated with solid lines. Angular grating structures are indicated with dashed lines. (c, d) TE_{00}-mode integrated dispersion (D_{int}) of resonators. Vertically dashed lines indicate resonances corresponding to zero-order OAM modes. Cross-section dimensions for the resonator waveguides are (a, c) 380 × 500 nm^2 and (b, d) 380 × 750 nm^2, respectively. (e) Comparison between the simulated and experimental group velocity dispersion of the TE_{00}-mode(f) TE_{00}-mode intrinsic $Q(Q_{int})$ histogram.

Microresonator design

Cross-section geometry of the resonator waveguides determines the intrinsic loss of the resonator and its dispersion. Importantly, the impact of angular gratings on the resonator performance (grating emission loss, and dispersion) is also heavily correlated to the waveguide cross-section geometry. Fig. S2(a,b) shows the mode profile of two different cross-section geometries. The narrower waveguide, shown in Fig. S2(a), exhibits larger field overlap with the grating structure than the wider waveguide, shown in Fig. S2(b). Although the size of the angular grating is identical in both waveguides, the narrower waveguide is influenced stronger due to its lower guided mode confinement and the larger width modulation (narrow waveguide: 5.7% modulation with 30-nm grating protrusion; wide waveguide: 3.8% modulation with 30-nm grating protrusion). Accordingly, the angular grating has stronger influence - dispersion perturbation and grating emission loss - to the narrower waveguide resonator system. Fig. S2(c,d) shows integrated dispersion (D_{int}) of the microresonators. The D_{int} is expressed as $D_{int} = \omega_\mu - (\omega_0 + D_1\mu)$, where μ is the longitudinal mode number, ω_μ is the resonance frequency of the μ-th WGM, ω_0 is the central frequency, and $D_1/2\pi$ is the FSR. We extract the D_{int} by collecting the terms in the parenthesis of the Taylor series expanded ω_μ, given as:
$\omega_\mu = \omega_0 + D_1\mu + (1/2 \cdot D_2\mu^2 + 1/6 \cdot D_3\mu^3 + ...)$

The D_{int} is expressed as:
$D_{int} = 1/2 \cdot D_2 \mu^2 + 1/6 \cdot D_3 \mu^3 + ...$
where D_2 is the second-order dispersion and D_3 is the third-order dispersion. The resonators exhibit pronounced avoided mode crossings (large resonant frequency deviations) in the resonances corresponding to the zero-order OAM modes, as indicated by the dashed lines in Fig. S2(c,d). This is attributed to a Bragg reflection (CW-CCW mode coupling) induced mode hybridization. Here, the narrow resonator waveguide (Fig. S2(c)) shows a larger frequency deviation compared to the wider counterpart (Fig. S2(d)), implying that the Bragg reflection from the grating structures is stronger for the narrower waveguide. Fig. S2(d) shows the group-velocity dispersion (GVD) of the waveguides determined by their cross-section dimensions. We show a strong geometric dispersion control where both anomalous (GVD>0) and normal (GVD<0) dispersion regimes can be achieved simply by varying the waveguide width. Fig. S2(e) shows intrinsic Q distributions of the resonators with two different waveguide cross-section widths. The intrinsic Q is determined by loss mechanisms that largely consist of waveguide surface scattering and angular grating scattering. We find that the resonators with the wider waveguide has a higher intrinsic Qs and less scattering strength.

Tuning FSR of the comb states

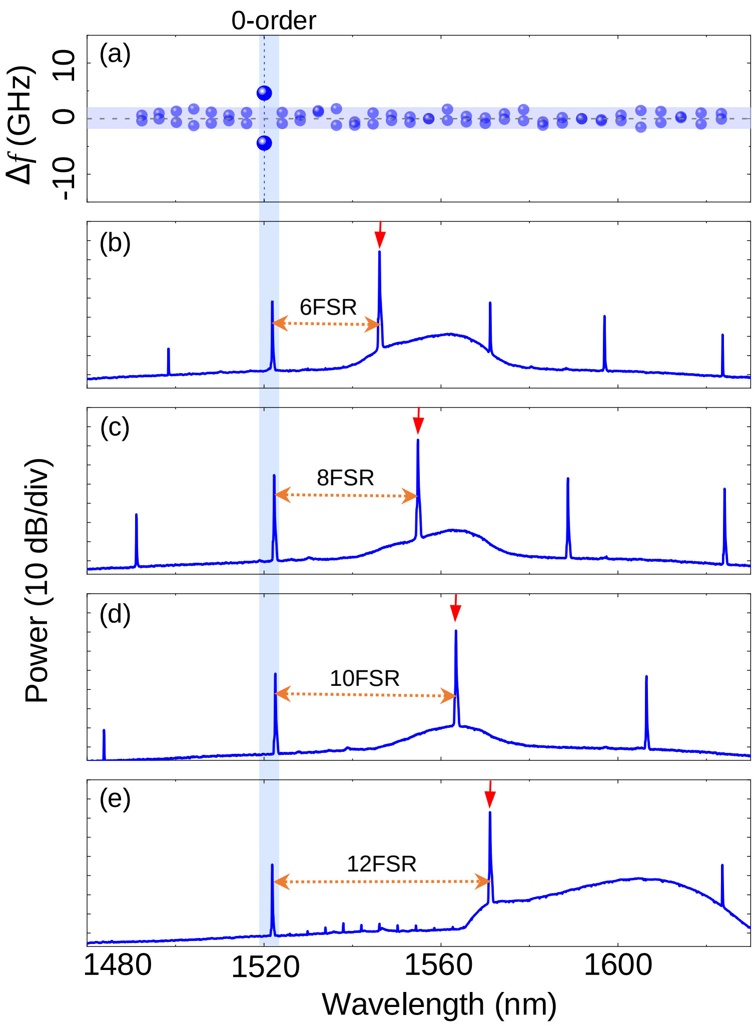

FIG. S3: **Comb initiation with different pumping conditions.** (a) Measured frequency deviation (Δf) of resonances with respect to the waveguide dispersion shown in Fig. S2(b). The pronouced large deviation occurs at the zero-order OAM resonance at around 1520 nm. (b-e) Measured Turing pattern comb spectra with different pumping wavelengths indicated by the red arrows.

The OAM microcomb has an inherent avoided mode crossing (AMX) at its zero-order OAM mode resonance, where the local dispersion can be tailored by tuning the grating modulation depth. Therefore, OAM microcombs can be generated in normal-dispersion microresonators without introducing extra mode hybridization using complex designs such as photonic molecules[2]. In addition, the free spectral range (FSR) of the Turing pattern can readily be changed by pumping at different resonances[3], as shown in Fig. S3. We find that the primary sidebands can be generated at the resonance for the zero-order OAM modes (indicated by the light blue shaded area) due to the inherent AMX of the vortex microcombs. Compared with the anomalous-dispersion microresonators, the normal-dispersion microresonators have enhanced pump-to-comb conversion efficiency by increasing the existence range of the Turing patterns without involving sub-comb generation. In that case, the mode-locking state can be maintained with multi-FSR-spacing turing patterns[4].

Cavity mode analysis

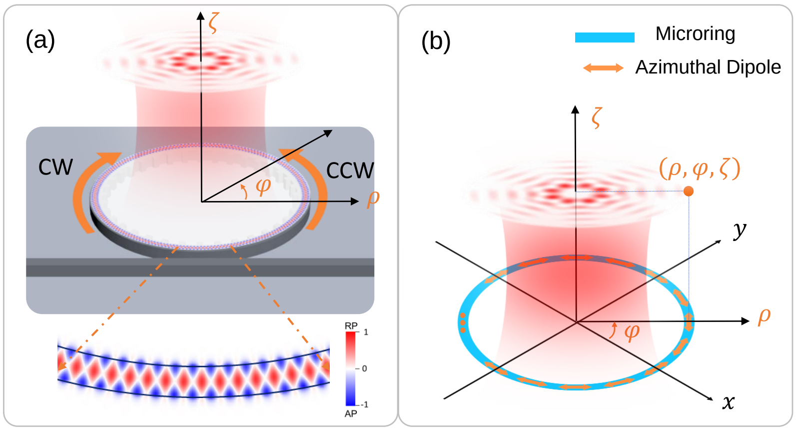

FIG. S4: (a) Schematic of the microring with inner wall embedded angular gratings emitting an interference pattern of CW and CCW modes carrying OAM. The simulation of radially polarized field and azimuthally polarized field confined in the microring resonator are denoted in red and blue respectively. (b) Schematic diagram of the dipole model in the cylindrical coordinate for far-field analysis.

Microring resonators can support whispering gallery modes (WGMs) carrying high-order OAM modes in which light is confined in the cavity by repeated total internal reflection[5,6]. In an ideal microring cavity, the clockwise (CW) mode and counter-clockwise (CCW) mode are frequency degenerate so that they have equal amplitudes but opposite topological charges of OAM. The propagation direction of the light in the coupling region determines which mode is excited. However, due to residual light scattering associated to the fabrication imperfections, the counter-propagating mode can also be significantly populated. As a result, these two counter-propagating modes interfere with each other and form standing wave patterns in the ring resonator. In high-index AlGaAs ring resonator with fixed number of grating elements, the quasi-transverse electric WGM with the dominant component $E_{\rho_{near}}$ distributes in the radially polarized (RP) direction, and the strong azimuthally polarized (AP) electric field, $E_{\varphi_{near}}$, exists at the ring waveguide sidewalls due to the tight mode confinement, as shown in Fig. S4(a). With the modulation of the sidewall gratings, the azimuthally polarized dipole radiation is a reasonable representation of the scattered field at each of the grating elements, which can be described by an azimuthal polarized dipole model in a cylindrical coordinate (ρ,φ,ζ), as shown in Fig. S4(b), the ρ and φ are the polar radius and azimuthal angles, ζ denotes the distance from microring plane normalized to the radius of the resonator. The following analytical results are based on this azimuthally polarized dipole model.

In the microring cavity, for a quasi-transverse WGM with the dominant electric field component being $E_{\rho_{near}}$ in the radial direction and $E_{\varphi_{near}}$ in the azimuthal direction, the far field components E_ρ and E_φ from the interference between the CW and CCW can be written as

$$E_\rho = E^{ccw}_{\rho,l} + e^{i\delta}E^{cw}_{\rho,-l} \tag{S1}$$

$$E_\varphi = E^{ccw}_{\varphi,l} + e^{i\delta}E^{cw}_{\varphi,-l} \tag{S2}$$

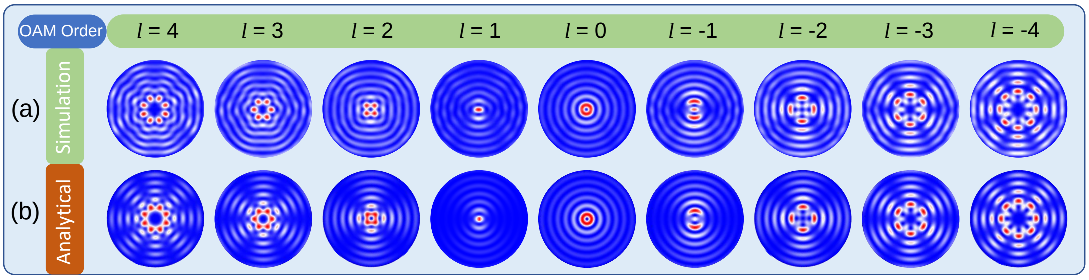

FIG. S5: (a) 3D FDTD simulated intensity distributions and (b) the analytical solutions of the far-field intensity distributions for the superposition modes from l = 4 to l = -4.

There is an initial phase difference of δ between E^{cw} and E^{ccw}, and a phase shift of $\pi/2$ between E_ρ and E_φ. As discussed in reference[7,8], within the framework of the paraxial approximation and in the far-field zone of dipole radiation, the transverse field components of azimuthally polarized dipoles for CCW can be expressed as

$$\mathrm{E}^{ccw}_{\rho,l} = (-i)^l \frac{A\nu^2\Phi(\rho,\zeta)}{\sqrt{\rho^2+\zeta^2}} e^{il\varphi}(J_{l+1}+J_{l-1}) \tag{S3}$$

$$\mathrm{E}^{ccw}_{\varphi,l} = (-i)^{l+1} \frac{A\nu^2\Phi(\rho,\zeta)}{\sqrt{\rho^2+\zeta^2}} e^{il\varphi}(J_{l+1}-J_{l-1}) \tag{S4}$$

where the constant $A = P_A q/8\pi\varepsilon_0 R^3$, the normalized propagation constant $\nu = 2\pi R/\lambda$, the propagation phase factor $\Phi(\rho,\zeta) = \exp[i\nu(2\zeta^2+\rho^2+1)/2\zeta]$, and $J_n = J_n(\nu\rho/\zeta)$ denotes the n^{th} order Bessel function of the first kind. In the case standing waves formed from a superposition of the CW and CCW modes, the total intensity distribution then becomes

$$\begin{aligned} |\mathrm{E}_T|^2 &= |\mathrm{E}_\rho|^2 + |\mathrm{E}_\varphi|^2 = |\mathrm{E}^{ccw}_{\rho,l} + e^{i\delta}\mathrm{E}^{cw}_{\rho,-l}|^2 + |\mathrm{E}^{ccw}_{\varphi,l} + e^{i\delta}\mathrm{E}^{cw}_{\varphi,-l}|^2 \\ &= \frac{4A^2\nu^4}{\rho^2+\zeta^2}[J^2_{l+1} + J^2_{l-1} + 2J_{l+1}J_{l-1}\cos(2l\varphi-\delta)] \end{aligned} \tag{S5}$$

The cosine item shows the standing wave characteristic in equation (5). With this far-field analytical solutions, we can plot the total intensity distribution. As shown in Fig. S5, the far-field patterns calculated from the analytical model agrees excellently with the simulations obtained from 3D FDTD simulations.

Methods to extract the OAM topological charges

Generally, the wavefront structure can be characterized by an interference scheme. In our experiment, the OAM nature can be confirmed by interfering the upwards-emitted photons with transmitted photons from the through port as a reference beam. The emitted vortices from the microring cavity are cylindrical vectorial beams, which can be described as the superposition of two orthogonal scalar vortices in circular polarization basis in the form of Jones matrices[9]

$$E_\rho = \frac{1}{2}\left[e^{i\theta(l+1)}\begin{pmatrix}1\\-i\end{pmatrix} + e^{i\theta(l-1)}\begin{pmatrix}1\\i\end{pmatrix}\right] \tag{S6}$$

$$E_\varphi = \frac{i}{2}\left[e^{i\theta(l+1)}\begin{pmatrix}1\\-i\end{pmatrix} - e^{i\theta(l-1)}\begin{pmatrix}1\\i\end{pmatrix}\right] \tag{S7}$$

Both E_ρ and E_φ consist of a right-hand circular polarized beam with a topological charge of $|l+1|$ and a left-hand circular polarized beam with a topological charge of $|l-1|$. As shown in Fig. S6(a,b), for the CCW radiated beams interferes with a co-propagating left-hand circularly polarized reference beam, spiral interference patterns can be clear observed with the number

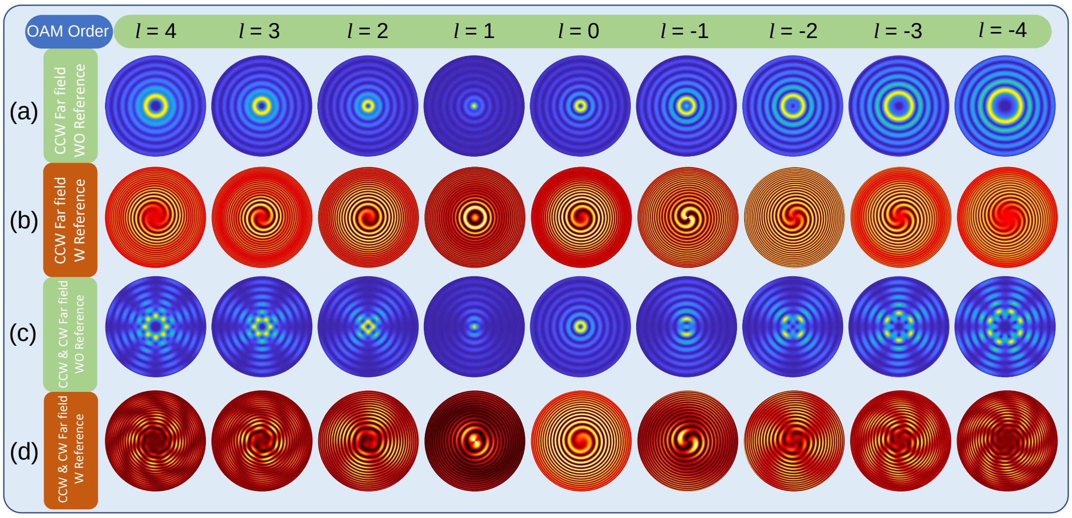

FIG. S6: (a) The far-field intensity distributions and (b) the interference patterns of OAM beams for CCW modes from l = 4 to l = -4. (c) The far-field intensity distributions and (d) the interference patterns for CW and CCW superposition modes from l = 4 to l = -4.

of arms equal to $|l-1|$. For the CW and CCW interference patterns, they are cylindrical vector modes as well. When projecting to the circular polarized basis, one can also observe $|l-1|$ spiral arms by interfering with left-hand circular polarized reference beams, as shown in Fig. S6(c,d).

For the far-field distribution, we can see that the radial and azimuthal components are superimposed together. Especially, for $l < 0$, the amplitudes of the radial and azimuthal components are strongly competing due to variation of the Bessel function in the analytical solutions[10], which leads to the hybrid RP/AP cylindrical vector vortices. In this scenario, it difficult to directly and quantitatively extract the topological charge for the high-order modes. We could resolve a separate radial pattern or angular pattern with an antinode number $n = 2|l|$ from equation (5), or $n = 2|l-1|$ for the x/y polarized patterns in Cartesian coordinate[8].

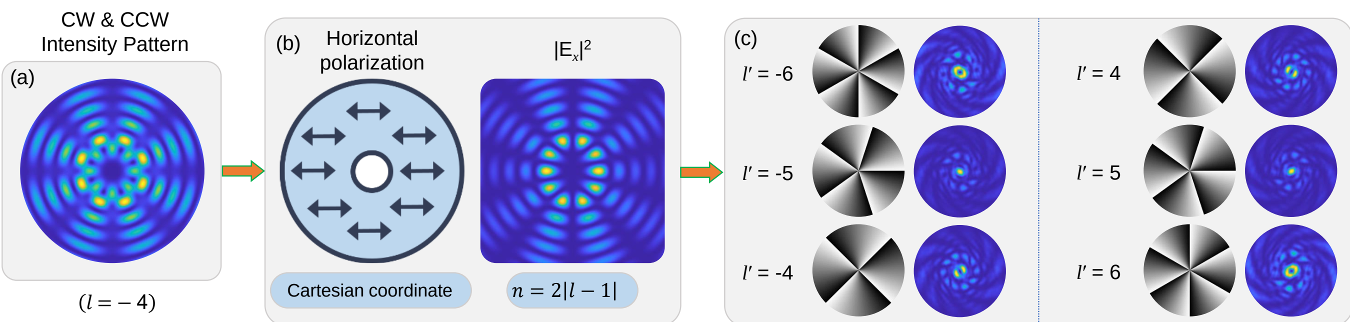

FIG. S7: (a) Simulated far-field intensity distributions of the CW and CCW interference pattern for l = - 4. (b) The far field pattern projected to the horizontal polarization (x component) in Cartesian coordinate with mode number $n = 2|l-1|$. (c) Simulations for the linear polarized OAM interference pattern projected to the holograms with l' = -6, -5, -4 and 4, 5, 6.

Experimentally, it is most straightforward to obtain the x/y component by simply using linear polarizers. For the beams passing through a linear polarizer along horizontal direction, we can derive the x component by a coordinate transformation $[\mathrm{E}_x = \mathrm{E}_\rho \cos(\varphi) - \mathrm{E}_\varphi \sin(\varphi)]$ from equations (3) and (4), so the electric field becomes

$$\mathrm{E}_x^l = (-i)^l \frac{A\nu^2\Phi(\rho,\zeta)}{\sqrt{\rho^2+\zeta^2}} [J_{l+1} e^{i(l+1)\varphi} + J_{l-1} e^{i(l-1)\varphi}] \tag{S8}$$

The corresponding far-field intensity distribution can be obtained as

$$\begin{aligned} I_{\text{Horizontal}} &= |E_x|^2 = |E_x^l + e^{i\delta} E_x^{-l}|^2 \\ &= \frac{2A^2 v^4}{\rho^2+\zeta^2}\,[J_{l+1}^2[(1+\cos(2(l+1)\varphi-\delta))] + J_{l-1}^2[(1+\cos(2(l-1)\varphi-\delta))] \\ &+2J_{l+1}J_{l-1}[\cos(2l\varphi-\delta)-\cos(2\varphi)]] \end{aligned} \tag{S9}$$

In such case, the topological charge can be determined by the anti-node number $n = 2|l-1|$. As shown in Fig. S7, taking l = - 4 as an example, when the interference pattern of CW mode and CCW mode projects to the linear polarization, we can clearly see 10 anti-nodes in the far-field pattern. In the main manuscript, we measured the high OAM orders from l = -5 to l = -13 by this method to extract the large topological charges. Furthermore, we can project the linear polarized interference pattern ($l = 4$) to the holograms to measure the purity of OAM modes and confirm the topological charge. Fig. S7(c) shows the simulations for the linearly polarized OAM interference pattern projected to the spatial light modulator (SLM) holograms with l' = -6, -5, -4 and 4, 5, 6, which exhibit bright spots in the center of the image when $l' = \pm|l-1|$. This demonstrates the two counter propagating modes CW and CCW coexist with opposite topological charges. With further mode analysis, we can obtain the mode purity of the emitted optical vortices, which is shown in the Fig. S9.

High-order OAM modes

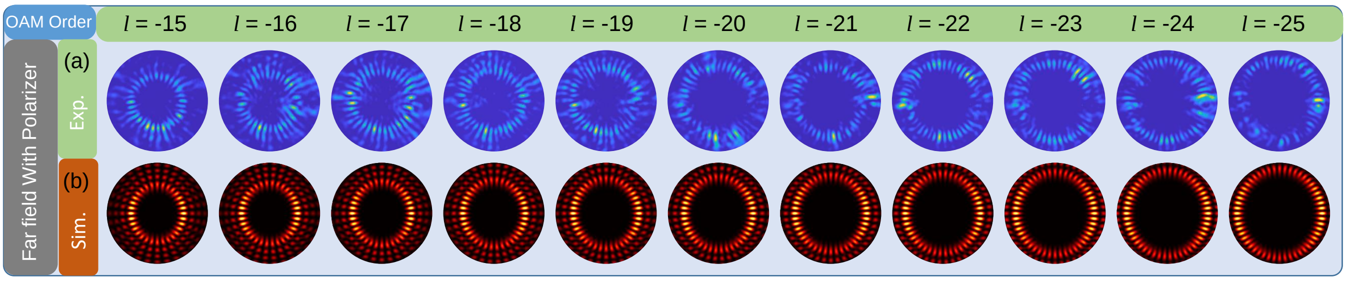

FIG. S8: The (a) measured and (b) simulated far-field patterns with linear polarizations for the emitted optical vortices with topological charges from -15 to -25.

We show that the high order OAM modes (l from -15 to 25) can also be reliably and identified by projecting the emitted photons to the linear polarization basis in Fig. S(8).

Measured OAM mode purity

OAM mode purity can be defined as the weight of the expected OAM mode intensity to the sum of all mode intensities contained in the OAM beam. For optical vortices generated from the microring, the purity of the modes consisting of both E_ρ and E_φ can be evaluated by converting either the right-hand or left-hand circularly polarized component to linearly polarized photons and then projecting them into SLM holograms with varied topological charge l'[11,12]. If the topological charge l' of the SLM hologram is opposite to the topological charge of the beam, then the resulting beam is of a planar phase front and thus can be focused by a lens to form an image with a bright spot in the center.

In Fig. S7(c), we have simulated the linearly polarized interference pattern projected to the holograms to extract the topological charges of the two counter propagating CW and CCW modes. As shown in Fig. S9(a), we projected the linearly polarized pattern to the SLM because it can only manipulate linearly polarized beams. With the SLM serving as a mode filter, an expected OAM mode would be extracted according to the helical phase masks on SLM. For the OAM modes from l = 4 to l = -4, as shown in Fig. S9(b), in each measurement of the linearly polarized component, the topological charge of the phase mask on SLM (l') are switched within the range of l' = -8 to 8 to extract the corresponding modes. We used the overlap integral method[13] to calculate the OAM spectrum of the beams by evaluating the radiated field intensity in the central area of the images (within a divergence angle of 5°). For the purity of the standing waves due to the CW and CCW interference, they exhibit bright spots in the center of the image when $l' = \pm|l-1|$ and most of the purity measurements are larger than 70%. Specially, when l = 1, only one bright spot occurred in the center of the image, the purity is about 80.3%. As detailed in Fig. S9(c-e), the linearly polarized component

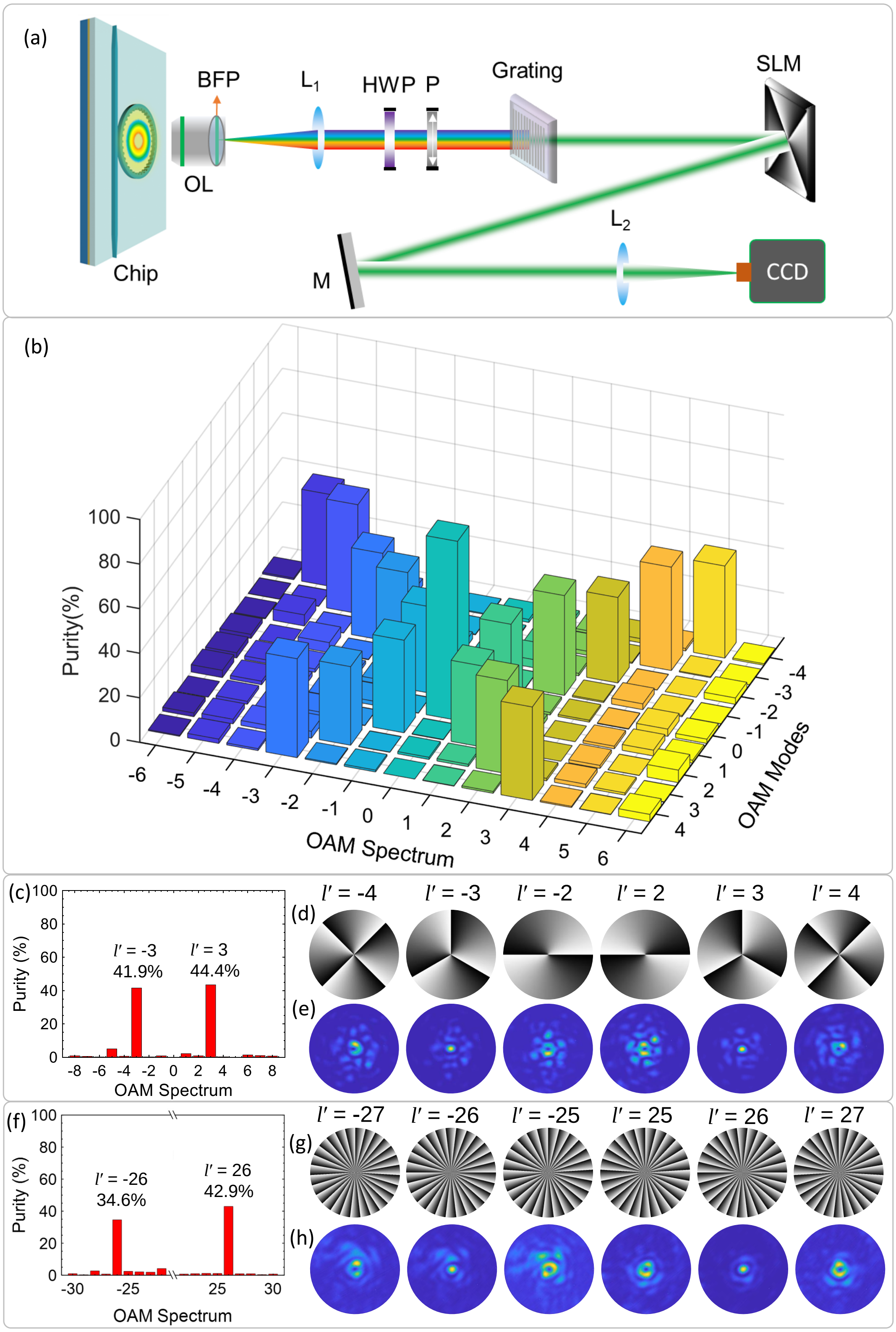

FIG. S9: **Measured OAM mode purity.** (a) Schematic of the experimental setup for the OAM mode purity measurement. OL: the objective lens, BFP: the back focal plane, HWP: half-wave plate, P: polarizer, SLM: spatial light modulator, M: mirror, L1 - L2: lenses, CCD: charge-coupled device. (b) OAM spectrum for OAM modes from l = 4 to l = -4. (c, f) Measured on-axis intensity distributions for the linearly polarized component of the emitted superposition mode with l = 4 and l = -25. (d, g) Phase distributions applied to the SLM. (e, h) Measured far-field patterns for the linearly polarized component of the superposition mode.

with a topological charge of l = 4 shows two main peaks of the on-axis intensities, corresponding to the holograms with l' = - 3 and 3. Thus, the topological charge of $l = \pm(|l'|+1)$ = 4 and - 4 was extracted for the emitted beams in OAM superposition modes. The mode energy is nearly equally distributed into l = 4 and - 4 with values of 41.9(1)% and 44.4(1)% of the total energy. By using this method, we could extract the higher order OAM modes and measure the mode purity. As shown in Fig. S9(f-h), it illustrates that the mode l = 25 and - 25 with a purity of about 34.6(1)% and 42.9(1)%, respectively.

Measured ejection efficiency

To estimate the ejection efficiency of the OAM modes, we fabricate a series of microrings with and without the grating modulation while keeping the other parameters fixed. (e.g. coupling gap, ring width, thickness, etc.) on the same chip. In the OAM cases, the total cavity linewidth is given by $\kappa_t = \kappa_t^0 + \kappa_e$, where κ_t^0 includes the contribution of the intrinsic loss rate κ_0 and the waveguide coupling rate κ_c, that is $\kappa_t^0 = \kappa_0 + \kappa_c$, and κ_e represents the coupling rate from the WGM mode to the free-space OAM mode, see Fig. S10(a). Given the tiny size of the grating and the identical fabrication process, we assume that the small variations in intrinsic Q and coupling Q between the OAM and reference cavities can be ignored, and attribute the broadened cavity linewidth to the extra coupling channel introduced by the grating, which gives an upper bound of the OAM ejection efficiency (κ_e/κ_t). The results are demonstrated in Fig. S10(b), where κ_e is calculated from the measured κ_t of the OAM cavity and κ_0 from the reference cavity[14]. The highest efficiency reaches 75.5%, at l = - 5. It is worth noting that the disparity of the efficiencies from mode to mode is related to the different nature of each WGM mode such as loaded Q and extinction ratio.

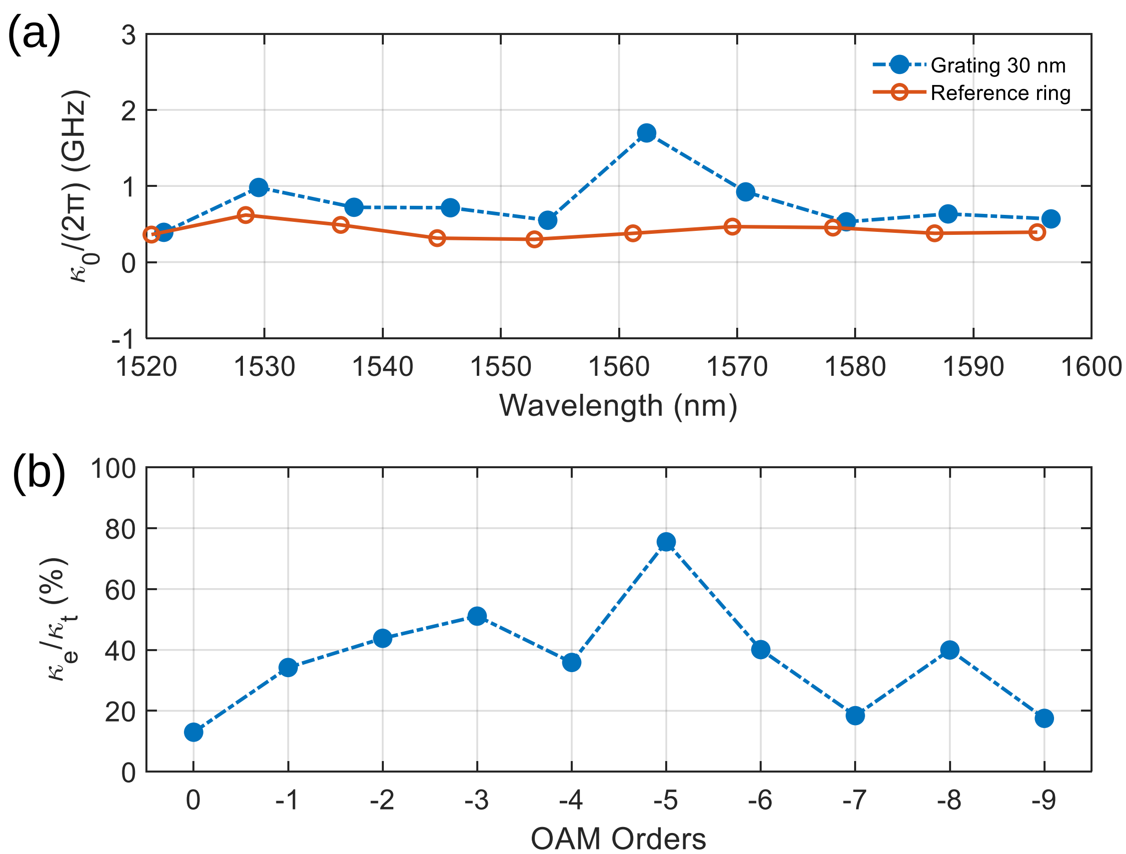

FIG. S10: (a) The comparison of intrinsic linewidth (κ_0) between the OAM cavity with grating size of 30 nm and the corresponding reference ring cavity. (b) Estimated OAM ejection efficiencies for the emitted optical vortices (κ_e/κ_t) with l varying from 0 to -9.

Self-torque pulse simulations

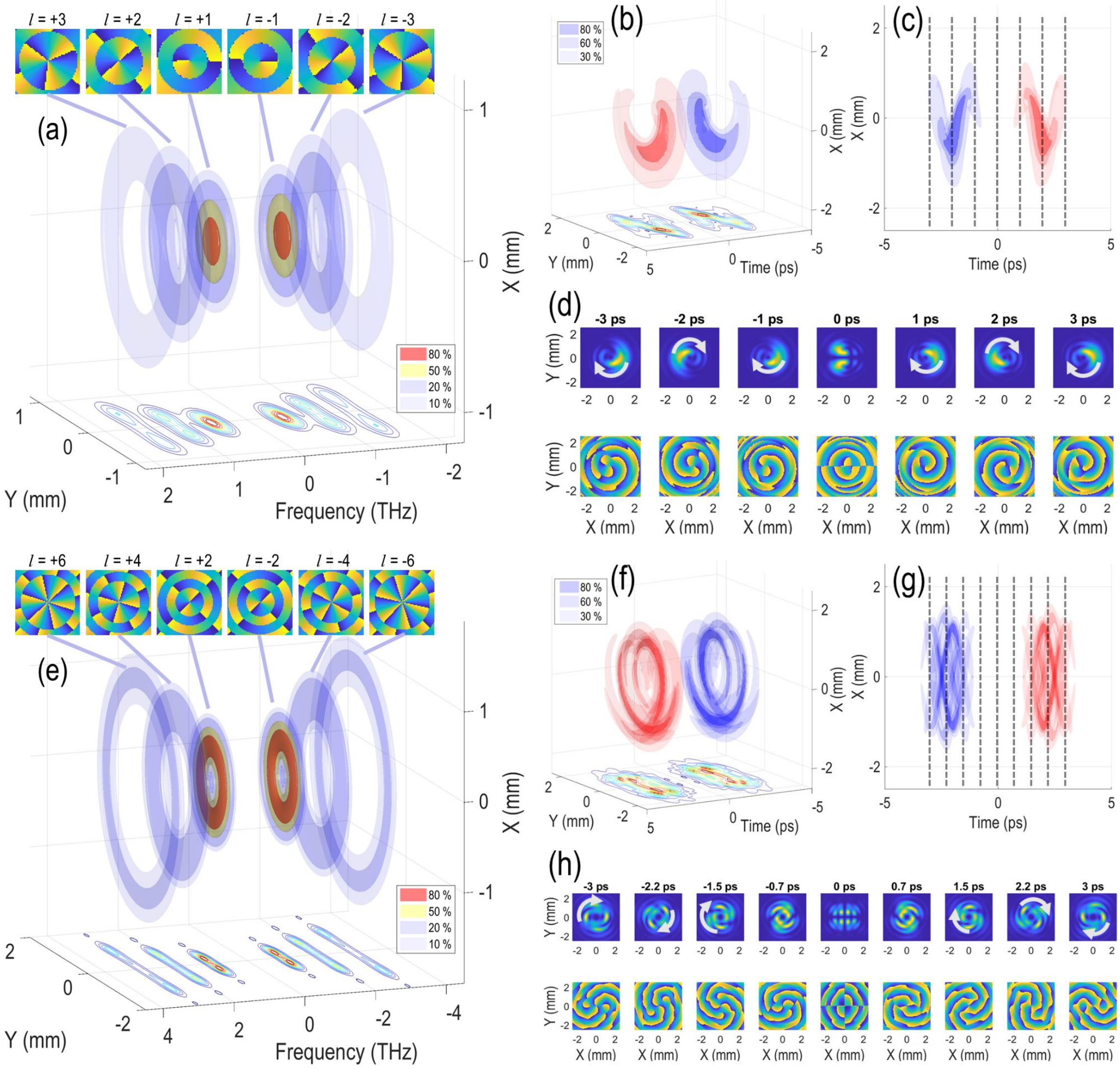

FIG. S11: **Simulations of the vortex microcombs operated in fundamental mode-locking state and harmonic (N = 2) mode-locking state.** (a), (e): Simulated comb modes in spatio-spectral domain. The insets show the phase profile of each mode. For fundamental mode-locking, the topological charge changes from -3 to +3. For harmonic mode-locking, the charge changes from -6 to +6. (b), (c), (f), and (g): ST profile of the self-torque pulses. The iso-surface color is registered to the sign of OAM carried by the self-torque pulse. (d), (h): Transverse cross-section of the self-torque pulse. For harmonic (N = 2) mode-locking, the self-torque pulse has a double-helix structure in ST domain.

The vortex microcomb can emit self-torque optical pulses with a time-varying OAM. We demonstrate such property of this spatiotemporal beams through numerical simulations. We simulate microcomb with 7 comb lines in radially polarization. According to ref.[7], the spatial profile of these comb modes in the far-field can be written as

$$\mathrm{E}_{\rho} \propto (-i)^{Nl} \frac{1}{\sqrt{\rho^2+\zeta^2}} e^{iNl\varphi} \left(J_{Nl+1}\left(\nu \frac{\rho}{\zeta}\right) + J_{Nl-1}\left(\nu \frac{\rho}{\zeta}\right) \right) \tag{S10}$$

where l is the topological charge of the comb mode and N is the harmonic order of the mode-locking state. In this study, we simulate two cases: microcombs operated in the fundamental mode-locking state (N = 1) and harmonic mode-locking state (N = 2). For fundamental mode-locking, the comb spacing equals to the FSR of the microring, which is 500 GHz. For harmonic mode-locking, the comb spacing equals to N times FSR, and, in this case, 1000 GHz. Fig. S11(a) and (e) illustrate the spatial-spectral profile of the simulated comb modes when the laser is fundamentally mode-locked and harmonically mode-locked. The

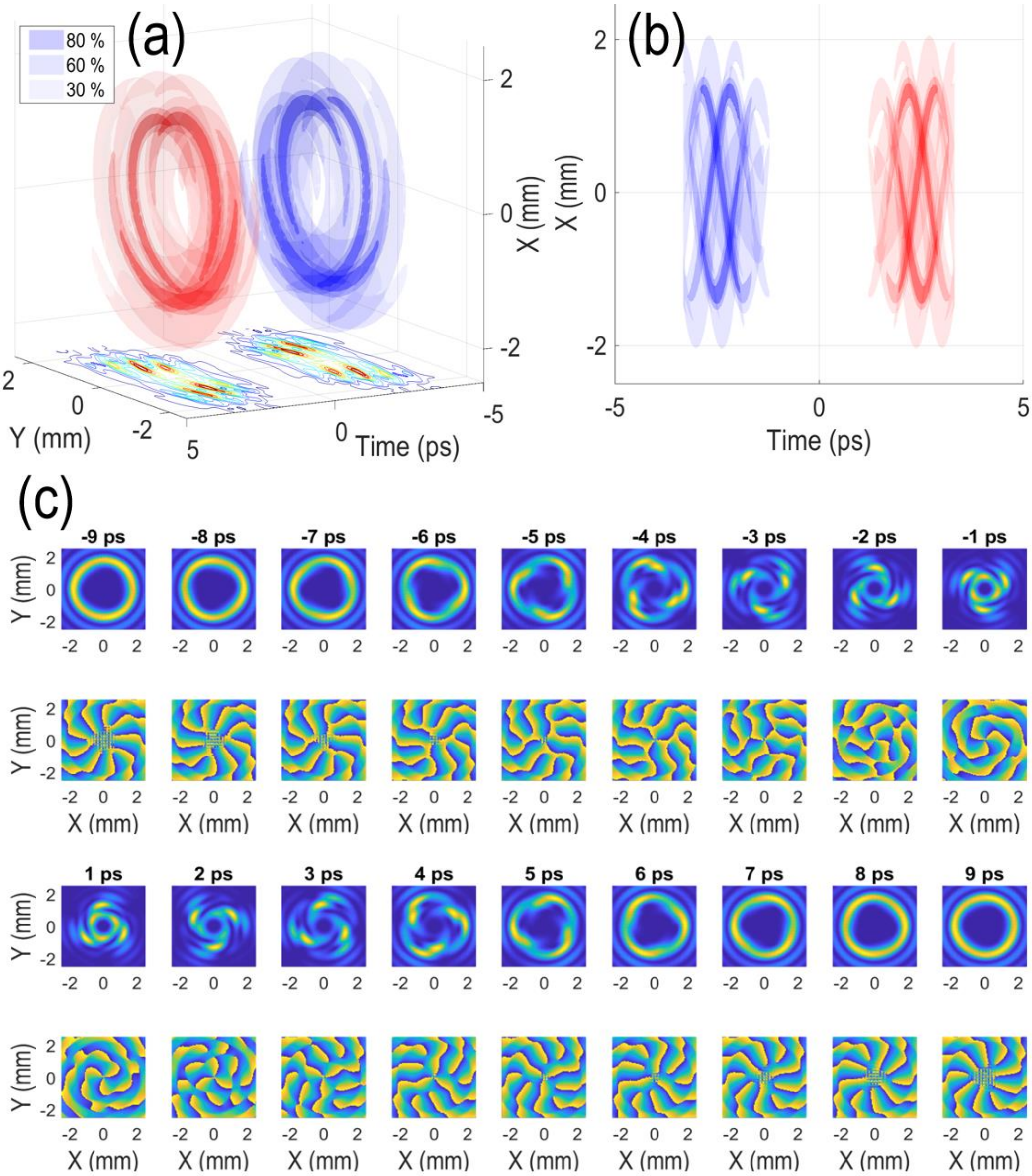

FIG. S12: **Simulation of the vortex microcomb operated in higher-order (N = 3) harmonic mode-locking state.** (a), (b): ST profile the self-torque pluses. (c): Cross-section of the self-torque pulse with triple helix structure in ST domain.

insets show the phase profile for each mode. For the fundamental mode-locking, topological charge carried by each mode varies from -3 to +3 with an interval of 1. For the harmonic mode-locking, topological charge varies from -6 to +6 with an interval of 2. In order to generate self-torque optical pulses, the vortex microcomb is phase modulated in the spectral domain. The applied spectral phase mask can be written as

$$\phi(\Omega) = \tau_0|\Omega| + \mathrm{GDD}\cdot\Omega^2 \tag{S11}$$

where $\Omega = \omega - \omega_0$, τ_0 is the linear phase coefficient, and GDD is the group delay dispersion (GDD) coefficient. such a phase modulation could be implemented experimentally by using a dispersive medium or a programmable pulse shaper. As shown in Fig. S11(b,c) and (f,g), the modulated laser output forms self-torque optical pulses in the spatiotemporal (ST) domain. The red/blue color of the isosurface plot indicates the positive/negative sign of OAM that is carried by the wavepacket. As already shown in the manuscript, the generated wavepacket has a time-varying OAM (Fig. 4). Besides, the temporal separation between two positive and negative OAM parts can be freely tuned by controlling the linear phase coefficient τ_0. In the case of harmonic mode-locking, the self-torque pulse features a double-helix structure in the ST domain, that is completely different compared with the self-torque pulse generated by HHG[15]. To further demonstrate the ST feature of self-torque pulses, we plot in Fig. S11(d) and (h) the cross-section of the pulse at different time. Fig. S11(h) clearly illustrates the double-helix structure of self-torque pulse generated by a vortex microcomb operated in the harmonic mode-locking regime. Moreover, the vortex microcomb can emit outputs in the form of triple or even higher order helix structure. To give an example, we show in Fig. S12 the ST feature of the vortex microcomb operated in N = 3 harmonic mode-locking regime, showing a clearly the triple-helix structure of the self-torque pulse.

---

* These authros contributed equally
† wangxueh@mail.sysu.edu.cn
‡ mipu@dtu.dk
§ liujin23@mail.sysu.edu.cn
[1] Chanju Kim, Chaochao Ye, Yi Zheng, Elizaveta Semenova, Kresten Yvind, and Minhao Pu. Design and fabrication of algaas-on-insulator microring resonators for nonlinear photonics. *IEEE J Sel Top Quantum Electron*, 2022.
[2] Óskar B Helgason, Francisco R Arteaga-Sierra, Zhichao Ye, Krishna Twayana, Peter A Andrekson, Magnus Karlsson, Jochen Schröder, and Victor Torres-Company. Dissipative solitons in photonic molecules. *Nat. Photon.*, 15(4):305–310, 2021.
[3] Yang Liu, Yi Xuan, Xiaoxiao Xue, Pei-Hsun Wang, Steven Chen, Andrew J Metcalf, Jian Wang, Daniel E Leaird, Minghao Qi, and Andrew M Weiner. Investigation of mode coupling in normal-dispersion silicon nitride microresonators for kerr frequency comb generation. *optica*, 1(3):137–144, 2014.
[4] Shu-Wei Huang, Jinghui Yang, Shang-Hua Yang, Mingbin Yu, Dim-Lee Kwong, Tanya Zelevinsky, Mona Jarrahi, and Chee Wei Wong. Globally stable microresonator turing pattern formation for coherent high-power thz radiation on-chip. *Phys. Rev. X*, 7(4):041002, 2017.
[5] Andrey B Matsko, Anatoliy A Savchenkov, Dmitry Strekalov, and Lute Maleki. Whispering gallery resonators for studying orbital angular momentum of a photon. *Phys. Rev. Lett.*, 95(14):143904, 2005.
[6] Xinlun Cai, Jianwei Wang, Michael J Strain, Benjamin Johnson-Morris, Jiangbo Zhu, Marc Sorel, Jeremy L O'Brien, Mark G Thompson, and Siyuan Yu. Integrated compact optical vortex beam emitters. *Science*, 338(6105):363–366, 2012.
[7] Jiangbo Zhu, Yujie Chen, Yanfeng Zhang, Xinlun Cai, and Siyuan Yu. Spin and orbital angular momentum and their conversion in cylindrical vector vortices. *Opt. Lett.*, 39(15):4435–4438, 2014.
[8] Bo Chen, Yuming Wei, Tianming Zhao, Shunfa Liu, Rongbin Su, Beimeng Yao, Ying Yu, Jin Liu, and Xuehua Wang. Bright solid-state sources for single photons with orbital angular momentum. *Nat. Nanotechnol.*, 16(3):302–307, 2021.
[9] Ignacio Moreno, Jeffrey A Davis, Isaac Ruiz, and Don M Cottrell. Decomposition of radially and azimuthally polarized beams using a circular-polarization and vortex-sensing diffraction grating. *Opt. Express*, 18(7):7173–7183, 2010.
[10] Jiangbo Zhu, Xinlun Cai, Yujie Chen, and Siyuan Yu. Theoretical model for angular grating-based integrated optical vortex beam emitters. *Opt. Lett.*, 38(8):1343–1345, 2013.
[11] Graham Gibson, Johannes Courtial, Miles J Padgett, Mikhail Vasnetsov, Valeriy Pas'ko, Stephen M Barnett, and Sonja Franke-Arnold. Free-space information transfer using light beams carrying orbital angular momentum. *Opt. Express*, 12(22):5448–5456, 2004.
[12] Michael J Strain, Xinlun Cai, Jianwei Wang, Jiangbo Zhu, David B Phillips, Lifeng Chen, Martin Lopez-Garcia, Jeremy L O'Brien, Mark G Thompson, Marc Sorel, et al. Fast electrical switching of orbital angular momentum modes using ultra-compact integrated vortex emitters. *Nat. Commun.*, 5(1):1–7, 2014.
[13] Yang Yue, Yan Yan, Nisar Ahmed, Jeng-Yuan Yang, Lin Zhang, Yongxiong Ren, Hao Huang, Kevin M Birnbaum, Baris I Erkmen, Sam Dolinar, et al. Mode properties and propagation effects of optical orbital angular momentum (oam) modes in a ring fiber. *IEEE Photon. J.*, 4(2):535–543, 2012.
[14] Xiyuan Lu, Mingkang Wang, Feng Zhou, Mikkel Heuck, Wenqi Zhu, Vladimir A Aksyuk, Dirk R Englund, and Kartik Srinivasan. Highly-twisted states of light from a high quality factor photonic crystal ring. *https://arxiv.org/abs/2208.13075*, 2022.
[15] Laura Rego, Kevin M Dorney, Nathan J Brooks, Quynh L Nguyen, Chen-Ting Liao, Julio San Román, David E Couch, Allison Liu, Emilio Pisanty, Maciej Lewenstein, et al. Generation of extreme-ultraviolet beams with time-varying orbital angular momentum. *Science*, 364(6447):eaaw9486, 2019.